PCCP

PAPER

View Article Online
View Journal | View Issue

Cite this: *Phys. Chem. Chem. Phys.*, 2019, **21**, 9895

Insights into how the aqueous environment influences the kinetics and mechanisms of heterogeneously-catalyzed COH* and CH_3OH* dehydrogenation reactions on Pt(111)†

Cameron J. Bodenschatz, Tianjun Xie,‡ Xiaohong Zhang‡ and Rachel B. Getman *

Received 10th February 2019,
Accepted 16th April 2019

DOI: 10.1039/c9cp00824a

rsc.li/pccp

Water influences catalytic reactions in multiple ways, including energetic and mechanistic effects. While simulations have provided significant insight into the roles that H_2O molecules play in aqueous-phase heterogeneous catalysis, questions still remain as to the extent to which H_2O structures influence catalytic mechanisms. Specifically, influences of the configurational variability in the water structures at the catalyst interface are yet to be understood. Configurational variability is challenging to capture, as it requires multiscale approaches. Herein, we apply a multiscale sampling approach to calculate reaction thermodynamics and kinetics for COH* dehydrogenation to CO* and CH_3OH* dehydrogenation to CH_2OH* on Pt(111) catalysts under liquid H_2O. We explore various pathways for these dehydrogenation reactions that could influence the overall mechanism of methanol decomposition by including participation of H_2O structures both energetically and mechanistically. We find that the liquid H_2O environment significantly influences the mechanism of COH* dehydrogenation to CO* but leaves the mechanism of CH_3OH* dehydrogenation to CH_2OH* largely unaltered.

1 Introduction

One of the grand challenges in catalysis research is understanding catalytic mechanisms. This is important since a molecular level understanding of catalytic chemistry can facilitate catalyst selection and design.[1,2] We are specifically interested in reactions that occur under aqueous phase. Examples of applications utilizing aqueous-phase conditions include aqueous-phase processing of biomass,[3–6] alcohol and acid fuel cells,[7–12] wastewater treatment,[13–17] and production of fine chemicals[3,18] and fuels.[18–20] Further, interest in using water as a "green" solvent in catalysis[21] motivates the need to understand how H_2O molecules influence catalytic chemistry.

Two of the primary ways in which water molecules influence catalytic mechanisms are altering the energies of catalytic species and participating in catalytic reactions. For example, water molecules interact with various chemical species adsorbed on solid catalyst surfaces through hydrogen bonding and van der Waals interactions.[22–41] These interactions have been shown to depend on the specific catalytic species and thus to influence reaction energies and activation barriers compared to gas phase. In some cases, they have been shown to depend on the specific arrangement of water molecules at the catalyst interface.[23,24,27,42–48] If significant enough, catalytic species interactions with liquid H_2O can alter dominant reaction pathways compared to gas phase.[24,31,41–43,49] Water can also participate in the reactions themselves. For example, water molecules can act as a source for surface hydrogen atoms and hydroxyl groups.[19,20,28,31,43,50] Further, H_2O molecules can mediate catalytic reactions, *e.g.*, by promoting cleavage of O–H bonds.[19,20,25–28,30–32,38,39,43,45,47,48,51–59]

While simulations have provided significant insight into the roles that H_2O molecules play in aqueous-phase heterogeneous catalysis, questions still remain as to the extent to which they influence catalytic mechanisms. One challenge is to properly sample the configurations (*i.e.*, the spatial arrangements) of the liquid H_2O molecules at the catalyst interface. Configurational variability arises due to temperature, and thus capturing it requires methods beyond quantum mechanics. *Ab initio* molecular dynamics (AIMD) addresses the finite temperature movements of liquid molecules; however, it is computationally intensive and thus limited in the number of configurations that can be generated.[56,60] Classical molecular dynamics (cMD) can generate liquid water

Department of Chemical and Biomolecular Engineering, Clemson University, Clemson, South Carolina 29634, USA. E-mail: rgetman@clemson.edu

† Electronic supplementary information (ESI) available: Calculation details for DFT and MD simulations including force field parameters, geometric criteria for hydrogen bonds and pre-exponential factor calculations, a comparison of implicit and explicit solvation results, structures of H_5O_2 and H_2O selected from an AIMD trajectory, and converged TS structures. See DOI: 10.1039/c9cp00824a

‡ These authors contributed equally to this work.

configurations in a more computationally tractable manner but cannot be used to model the breaking and forming of chemical bonds. Alternatively, reactive force fields can capture bond breaking and forming;[61–63] however, reactive force fields are available for a limited number of heterogeneously catalyzed systems. Capturing the influence of configurational variability on catalytic energetics (reaction energies, activation energies) thus requires combining methods that can capture sufficient numbers of configurations as well as the energetics of bond breaking and forming. Calculating rate constants for catalytic reactions in liquid H_2O also requires new methods,[64] as present methods rely on theories based on the assumption that the reaction environment is an ideal gas[43] (and thus are independent of the configuration of fluid phase molecules at the catalyst interface).

Our goal in this work is to improve insight about how the configurational variability of the liquid structure influences catalytic mechanisms. We are specifically interested in comparing reactions involving polar *versus* non-polar reaction intermediates, which we expect to exhibit different behaviors in water. To explore such phenomena, we model Pt(111)-catalyzed hydroxymethylidyne dehydrogenation to carbon monoxide, *i.e.*, $COH^* + * \rightarrow CO^* + H^*$, and methanol dehydrogenation to hydroxymethyl, *i.e.*, $CH_3OH^* + * \rightarrow CH_2OH^* + H^*$. These reactions were chosen because they allow comparison of catalytic O–H *versus* C–H cleavage, which serve as examples for H_2O participation with hydrophilic *versus* hydrophobic functional groups, and because they are expected to be part of the dominant reaction pathway in methanol decomposition.[65] To capture the configurational variability, we combine cMD with density functional theory (DFT), in an approach that we recently coined "multiscale sampling".[60] This method enables the generation of realistic liquid water structures for calculating catalytic quantities. These types of calculations are not possible with DFT or cMD by themselves. We use the multiscale sampling approach to calculate reaction energies, activation barriers, and pre-exponential factors for the COH^* and CH_3OH^* dehydrogenation reactions. Comparing the results for the analogous reactions under vacuum, we provide the most conclusive results to date of the roles of liquid H_2O molecules on the reaction energies, activation barriers, and pre-exponential factors involved in the COH^* and CH_3OH^* dehydrogenation reactions on Pt(111). Our results show that the liquid H_2O environment significantly influences the thermodynamics and kinetics of the COH^* dehydrogenation step but has a much more minor influence on the thermodynamics and kinetics of the CH_3OH^* dehydrogenation step.

2 Methods

2.1 Reaction pathways

The catalytic dehydrogenations of COH^* and CH_3OH^* were modeled in three different pathways. The first is "direct" dehydrogenation, where the H atom is transferred directly from the reactant to the catalyst surface, *e.g.*,

$$COH^* + * \rightarrow CO^* + H^* \quad (1)$$

where the * indicates a vacant binding site on the Pt(111) surface and *'ed species are bound to the catalyst surface. The second and third pathways involve liquid H_2O molecules and thus require a model for such. While prior literature has shown that at low temperature (<145 K), H_2O molecules arrange in hexagonal, ice-like patterns on metal surfaces,[66–69] it is not well-understood how liquid H_2O molecules adsorb to metal surfaces. Competition between hydrogen bonding, interactions with the metal surface atoms, and thermal fluctuations complicate experimental and computational attempts to visualize a H_2O molecule reaction intermediate. In our MD simulations (including cMD and AIMD), we have observed that H_2O molecules near the Pt surface that are not hydrogen bonded to catalytic species remain more fluid-like than chemically adsorbed reaction intermediates and transition states. That is, H_2O molecules near the surface demonstrate more significant thermal fluctuations in their spatial positions. Hence, we treat such H_2O molecules as fluid phase species (*i.e.*, that do not participate in the site balances) in the chemical equations presented below. To participate in a chemical reaction, we assume that a liquid H_2O molecule near the Pt surface first forms a complex with a reaction intermediate. In these complexation reactions, a near-surface H_2O molecule interacts with a catalytic species through van der Waals interactions and/or hydrogen-bonding, and this interaction lasts for a specified amount of time (*i.e.*, the interaction is not fleeting). The specific requirements are elaborated in Section 2.3. For example, the complexation of COH^* with a liquid H_2O molecule near the Pt surface is written as

$$COH^* + H_2O \rightarrow COH\text{–}H_2O^* \quad (2)$$

In a subsequent step, the complexed H_2O molecule can either "co-catalyze" the dehydrogenation,[45,57,70] *e.g.*,

$$COH\text{–}H_2O^* + * \rightarrow CO^* + H^* + H_2O \quad (3)$$

or "assist" the dehydrogenation. We model the assisted pathway as involving complexation of a second water molecule, *e.g.*,

$$COH\text{–}H_2O^* + H_2O \rightarrow COH\text{–}H_2O\text{–}H_2O^* \quad (4)$$

followed by cleavage of the C–H or O–H bond to form H_5O_2, *e.g.*,

$$COH\text{–}H_2O\text{–}H_2O^* \rightarrow CO^* + H_5O_2 \quad (5)$$

Here, we use the H_5O_2 species as a general model of $H_{2n+1}O_n$ species. Values of n have been shown to vary from 1[30,39,70,71,72] to 6,[73] depending on the system. We chose H_5O_2 as a model for $H_{2n+1}O_n$ species since our test calculations show that reaction energetics involving $H_{2n+1}O_n$ species are reasonably converged when $n = 2$. More details about these tests are provided in Section S11 of the ESI.†

Analogous reactions for dehydrogenation of methanol to hydroxymethyl are

$$CH_3OH^* + * \rightarrow CH_2OH^* + H^* \quad (6)$$

$$CH_3OH^* + H_2O \rightarrow CH_3OH\text{–}H_2O^* \quad (7)$$

$$CH_3OH\text{–}H_2O^* + H_2O \rightarrow CH_3OH\text{–}H_2O\text{–}H_2O^* \quad (8)$$

and

$$CH_3OH–H_2O–H_2O^* \rightarrow CH_2OH^* + H_5O_2 \quad (9)$$

respectively, with the exception that we neglected the co-catalyzed pathway because its pre-exponential factor is prohibitively small (see Section 3.4). To complete the H_2O-assisted pathways for both the CH_3OH^* and COH^* reactants, we also modeled H_5O_2 dehydrogenation, *i.e.*,

$$H_5O_2 + * \rightarrow 2H_2O + H^* \quad (10)$$

Over the course of the catalytic cycle, a H species is abstracted from a reaction intermediate and deposited on the Pt(111) surface. We generally refer to these species as "hydrogen atoms" in this work; however, we note that these species could alternatively be protons.

2.2 Reaction energies and activation energies

Aqueous phase reaction energies were calculated as in prior work,[42,43] *i.e.*:

$$\Delta E_{rxn}^{aq} = \Delta E_{rxn}^{vac} + \Delta\Delta E_{int} \quad (11)$$

where ΔE_{rxn}^{aq} is the reaction energy calculated under liquid water, ΔE_{rxn}^{vac} is the reaction energy calculated under vacuum, and $\Delta\Delta E_{int}$ is the difference in the calculated water–adsorbate interaction energy between products and reactants. For example, ΔE_{rxn}^{vac} for reaction (1) is calculated as $\Delta E_{rxn}^{vac} = E^{vac}(CO^*) + E^{vac}(H^*) - E^{vac}(COH^*) - E^{vac}(*)$, and ΔE_{int} for COH^* is calculated as $\Delta E_{int}(COH^*) = E^{aq}(COH^*) + E^{vac}(*) - E^{vac}(COH^*) - E^{aq}(*)$.[23] ΔE_{int} are reported as averages over 10 configurations of liquid H_2O molecules generated using the multiscale sampling approach, plus or minus the 95% confidence interval. More details about the multiscale sampling method are included in Section S6 of the ESI.† $\Delta\Delta E_{int}$ is then calculated by subtracting the interaction energies of the reactants from those of the products, *e.g.*, $\Delta\Delta E_{int} = \Delta E_{int}(CO^*) + \Delta E_{int}(H^*) - \Delta E_{int}(COH^*) - \Delta E_{int}(*)$. Activation energies were calculated analogously,[43] *i.e.*,

$$\Delta E_{act}^{aq} = \Delta E_{act}^{vac} + \Delta\Delta E_{int} \quad (12)$$

where $\Delta\Delta E_{int}$ in this case is calculated by subtracting the interaction energy of the reactants from that of the transition state. ΔE_{act}^{aq} for complexation reactions (2), (4), (7), and (8) were assumed to be low (below k_BT) because they do not involve re-arrangements of chemical bonds, and thus we set them equal to zero in this work.

2.3 Pre-exponential terms

Pre-exponential factors for reactions (1), (3), (5), (6) and (9), which all involve O–H or C–H bond breaking, were approximated as equal to k_BT/h, where k_B is Boltzmann's constant and h is Planck's constant.

Reactions (2) and (7) involve complexation of a H_2O molecule with a catalytic species. To help discern the influence of configurational variability in the H_2O structure on the kinetics of these reactions, we estimated their pre-exponential factors from cMD trajectories as the number of occurrences per unit time that the H_2O structure (1) oriented in a way so as to promote the complexation and (2) held for 0.16 ps using the structural criteria presented below. This procedure was inspired by the work of Savara and coworkers.[64] The time requirement of 0.16 ps is equal to h/k_BT at the simulation temperature of 300 K, which is approximately equal to the period of a molecular vibration at that temperature. If the H_2O structure held for more than 0.16 ps, then it was counted toward the pre-exponential factor in 0.16 ps increments until it was deemed that it could no longer promote the complexation reaction of interest. In this strategy, a H_2O structure that could continuously promote complexation of a H_2O molecule and a COH^* or CH_3OH^* species would have a pre-exponential factor equal to k_BT/h. A water structure was deemed able to promote a complexation reaction when the distance between the O atom on one of the liquid H_2O molecules and the O or C atom in the relevant –OH or –CH functional group was $\leq$3.5 Å and the corresponding O_{H_2O}–O–H or O_{H_2O}–C–H angle was $\leq 30^\circ$. These criteria were adopted from the established geometrical criteria for hydrogen-bonding (see Section S2 of the ESI†).[74,75] However, they only identify the frequency at which reactant–H_2O complexes form. To further distinguish H_2O complexes that could promote co-catalyzed dehydrogenation reactions (which represent a fraction of the total), we included two more criteria involving the orientation of the specific H_2O molecule that complexed with the reactant adsorbate. Specifically, to co-catalyze a dehydrogenation reaction, the H_2O molecule in the complex must comprise a "dangling" hydrogen atom,[56] *i.e.*, which points toward the Pt(111) surface. To capture these specific configurations, we counted structures where the c coordinate of an H atom from the H_2O molecule was below the c coordinate of the water O atom and where the distance in the c dimension between this H atom and the Pt surface plane was $\leq$2.5 Å. These criteria are illustrated in Fig. S2 in the ESI.† The pre-exponential factors estimated from structural criteria are presented as averages over at least 5 cMD trajectories, plus or minus the 95% confidence intervals.

Reactions (4) and (8) involve complexation of a second H_2O molecule to a reactant–H_2O complex. Since in our cMD simulations liquid water is almost continuously structured so as to promote complexation of two H_2O molecules, we set the pre-exponential factors of these reactions equal to k_BT/h.

2.4 Details of the multiscale sampling procedure

The multiscale sampling procedure is illustrated as a flowchart in Fig. S8 in the ESI.†

2.4.1 Simulation boxes. Pt(111) catalysts were modeled using slabs comprised of three-layer 3 Pt × 3 Pt periodic surfaces (*i.e.*, containing 27 total Pt atoms) in monoclinic $p(3 \times 3)$ supercells with dimensions of $a = b = 8.416$ Å and angles of $\alpha = \beta = 90.0^\circ$ and $\gamma = 60.0^\circ$. The (111) surface was created by cutting a slab from the structure of bulk Pt, which has a calculated lattice constant of 3.967 Å (compared to the experimental value of 3.924 Å[76]). Reaction intermediates and transition state (TS) complexes were adsorbed to the top surface layer. The total coverage of reaction intermediates or TSs (not including liquid H_2O molecules) was held constant at 1/9

monolayer (ML), where 1 ML is equal to 1 reaction intermediate or TS complex per surface metal atom. Liquid water was simulated by including up to 24 H_2O molecules above the top Pt(111) surface layers. Configurations of these H_2O molecules around reaction intermediates and TS complexes were obtained as follows. First, reaction intermediate and TS complex geometries were obtained following the procedures described in Section 2.4.2. Since reaction intermediates and TS complexes could contain one or two H_2O molecules, additional H_2O molecules were added to the supercells so that the total number of H_2O molecules in each supercell was equal to 24. The trajectories of all of the H_2O molecules that were *added to* the supercells were simulated in cMD (Section 2.4.3), while the geometries of the reaction intermediates and TS complexes (including any involved H_2O molecules) and all Pt atoms were held fixed. In cMD simulations, the supercell *c* dimension was equal to 24.524 Å, giving a total supercell volume of 1505 $Å^3$ and a bulk water density of $\sim$ 1 g cm^{-3}. Configurations of H_2O molecules were selected from the cMD trajectory and then partially re-optimized in DFT (Section 2.4.4). In DFT calculations, an additional 14 Å of vacuum space was added above the top of the liquid H_2O structure, yielding a total *c* dimension of 38.524 Å, to minimize interactions between neighboring periodic images. Since only small perturbations were made to the liquid water structure in the DFT calculations (see Section 2.4.4), this addition had a negligible effect on the water density local to the catalytic surface.

2.4.2 Geometries of reaction intermediates and transition state complexes for use in cMD. Geometries of reaction intermediates for use in cMD were obtained using geometry relaxations performed in DFT under vacuum, and geometries of TS complexes for use in cMD were obtained in DFT under configurations of liquid H_2O molecules (see Section 2.4.4), with the exceptions of the H_2O and H_5O_2 reaction intermediates and the TS complexes for the H_2O-assisted COH* dehydrogenation and H_5O_2 dehydrogenation reactions (reactions (5) and (10)), which were generated from AIMD trajectories. These simulations were initiated from configurations sampled from cMD trajectories[60] and were performed in the canonical (*NVT*) ensemble at 300 K, maintained with the Nosé–Hoover thermostat.[77,78] Two total AIMD simulations were performed, one on a solvated COH* species, and one on a solvated H_5O_2 species. During the AIMD trajectories, the COH* and H_5O_2 species were observed to dehydrogenate to CO* + H_5O_2 and $2H_2O$ + H*, respectively. TS structures for use in cMD were taken from the respective occurrences in the AIMD trajectories. Geometries of the H_2O and H_5O_2 reaction intermediates were generated from the trajectory of the solvated H_5O_2 species. Further details about the AIMD simulations are provided in Section S4 the ESI.†

2.4.3 Classical MD simulations. cMD simulations were performed in the *NVT* ensemble using the Large-scale Atomic/Molecular Massively Parallel Simulator (LAMMPS).[79] The target temperature was set to 300 K, which was maintained with the Nosé–Hoover thermostat.[77,78] The timestep was 1 fs, and atomic positions were reported every 100 fs. Intermolecular energies were calculated with Lennard-Jones + Coulomb (LJ + C) potentials. LJ parameters for Pt atoms were taken from the universal force field (UFF)[80] and partial charges on Pt atoms were set to zero. LJ and C parameters for reaction intermediates were taken from the Optimized Potentials for Liquid Simulations (OPLS-AA)[81] force field, while those for water were taken from the Transferable Intermolecular Potential with 3 Points-Chemistry at Harvard Macromolecular Mechanics[82] (TIP3P-CHARMM) force field. Cross-terms for the LJ interactions were calculated using Lorentz–Berthelot mixing rules.[83,84] This model of H_2O interacting with the catalytic surface is discussed further in Section S5 of the ESI,† including comparison with more detailed models. Water molecules were simulated as flexible in our cMD simulations, with bond and angle force constants and equilibrium bond lengths and angles taken from the TIP3P-CHARMM force field.[82] The cMD simulations were carried out for a total of 5 ns, where the first 2 ns were used for system equilibration and the remaining time was used to generate configurations of liquid H_2O molecules. Configurations of liquid H_2O molecules were selected at time intervals of at least 300 ps during the last 3 ns of the cMD runs. The 300 ps time interval was chosen because it is significantly longer than the longest ''lifetime'' of a hydrogen bond formed between a liquid H_2O molecule and a reaction intermediates (110 ps, for the COH* intermediate[85]).[60]

2.4.4 DFT calculations. DFT calculations were performed using the Vienna *Ab initio* Simulation Package (VASP),[86–89] which employs planewave basis sets and periodic boundary conditions. Energies of core elections were modeled using projector augmented-wave (PAW) pseudopotentials[90,91] to a cut-off energy of 400 eV, and exchange and correlation of valence electrons were modeled using the Perdew–Burke–Ernzerhof (PBE) functional.[92,93] The D2 dispersion correction[94] was used to improve the modeling of dispersion. Gaussian smearing with a smearing factor of 0.1 eV was used to set the partial occupancies of each orbital. The first Brillouin zones were sampled using automatically-generated 7 × 7 × 1 Monkhorst–Pack *Γ*-centered *k*-point meshes.[95] Electronic structures were converged self-consistently until the difference in energy between subsequent iterations was no larger than 10^{-5} eV. Geometry relaxations for catalytic intermediates were performed using a force-based quasi-Newton algorithm.[96] In geometry relaxations performed under vacuum (for use in cMD), the reaction intermediates was allowed to relax, while all Pt atoms were held fixed. In geometry relaxations performed under configurations of liquid water (which were generated in cMD), geometries of any H_2O molecules that were hydrogen bonded to the reaction intermediates were allowed to relax, while the geometries of the reaction intermediates, all other H_2O molecules, and all Pt atoms were held fixed. Test simulations indicated that different relaxation strategies influenced interaction energies by $<$0.1 eV. More information about the relaxation strategies tested is included in Section of S7 the ESI.† TS searches were performed using a combination of the climbing image-nudged elastic band[97,98] (CI-NEB) and dimer[99] methods under configurations of liquid H_2O generated in cMD. Further details about how the configurations were generated are provided in Section S9 of the ESI.† CI-NEB simulations were performed using seven discrete images along the reaction coordinate (the initial and final images plus five intermediate images) connected with ''springs'' with force constants equal to 5 eV $Å^{-2}$. The five intermediate images were relaxed in CI-NEB toward the minimum energy path (MEP) until the

maximum force on all non-fixed atoms in all directions other than the reaction coordinate fell below 0.5 eV $Å^{-1}$. A guess of the TS geometry was then generated from the resulting images using the neb2dim.pl script from Henkelman's website,[100] and this structure was relaxed to a first order saddle point using the dimer method.[99] The convergence criterion for all geometry relaxations and transition state searches reported herein was that the maximum force on all of the non-fixed atoms be less than or equal to 0.03 eV $Å^{-1}$. The structures of all TS complexes reported in this work were verified using vibrational mode analysis (details provided in Section S9 of the ESI†).

3 Results

3.1 Structures and interaction energies of reaction intermediates

Calculated structures of COH*, CO*, CH_3OH*, CH_2OH*, H_2O, H_5O_2, COH–H_2O*, COH–H_2O–H_2O*, CH_3OH–H_2O*, and CH_3OH–H_2O–H_2O* are shown in Fig. 1, and calculated values of ΔE_{int} are given in Table 1. Further, ΔE_{int} are compared with implicit solvation in Section S1.1 of the ESI.† Interaction energies are all negative (except for H*, for which ΔE_{int} is 0), indicating favorable interaction with liquid H_2O. Values range from -0.03 ± 0.03 eV for CO* to -1.50 ± 0.31 eV for H_5O_2. The catalytic species with hydroxyl groups (all except CO* and H*) have larger (more negative) interaction energies. For example, the interaction energy of COH* (Fig. 1a) is -0.70 eV, meaning that the interaction with H_2O stabilizes COH* on the Pt surface by -0.70 eV. Further, ΔE_{int} are stronger for species where the hydroxyl groups are sterically accessible to the liquid H_2O environment. For example, the ΔE_{int} for CH_2OH* (Fig. 1d) is stronger at -0.65 ± 0.12 than for CH_3OH* (Fig. 1c) at -0.48 ± 0.18 because the –OH group on CH_2OH* points up into the liquid H_2O environment, whereas the –OH group on CH_3OH* points toward the Pt(111) surface. Similar comparisons can be made for H_5O_2 (Fig. 1f) *versus* H_2O (Fig. 1e), CH_3OH–H_2O* (Fig. 1i) *versus* COH–H_2O* (Fig. 1g), and CH_3OH–H_2O–H_2O* (Fig. 1j) *versus* COH–H_2O–H_2O* (Fig. 1h).

3.2 Calculated reaction energies

Calculated reaction energies are reported in Table 2 and plotted in Fig. 2. They include contributions from the energy due to the breaking and forming of chemical bonds (ΔE_{rxn}^{vac}) as well as from the change in the water–adsorbate interaction ($\Delta\Delta E_{int}$). Reactions where the aqueous environment stabilizes the reactant state more than the product state have a positive $\Delta\Delta E_{int}$ and are therefore less thermodynamically favorable than their vacuum-phase analogues. Reactions (1) (*i.e.*, COH* + * → CO* + H*), (2) (*i.e.*, COH* + H_2O → COH–H_2O*), (3) (*i.e.*, COH–H_2O* + * → CO* + H* + H_2O), (8) (*i.e.*, CH_3OH–H_2O* + H_2O → CH_3OH–H_2O–H_2O*), and (10) (*i.e.*, H_5O_2 + * → 2H_2O + H*) fall into this category. Conversely, reactions where the water environment stabilizes the product state more than the reactant state have a negative $\Delta\Delta E_{int}$ and are therefore more thermodynamically favorable than their vacuum-phase analogs. Reactions (4) (*i.e.*, COH–H_2O* + H_2O → COH–H_2O–H_2O*), (5) (*i.e.*, COH–H_2O–H_2O* → CO* + H_5O_2),

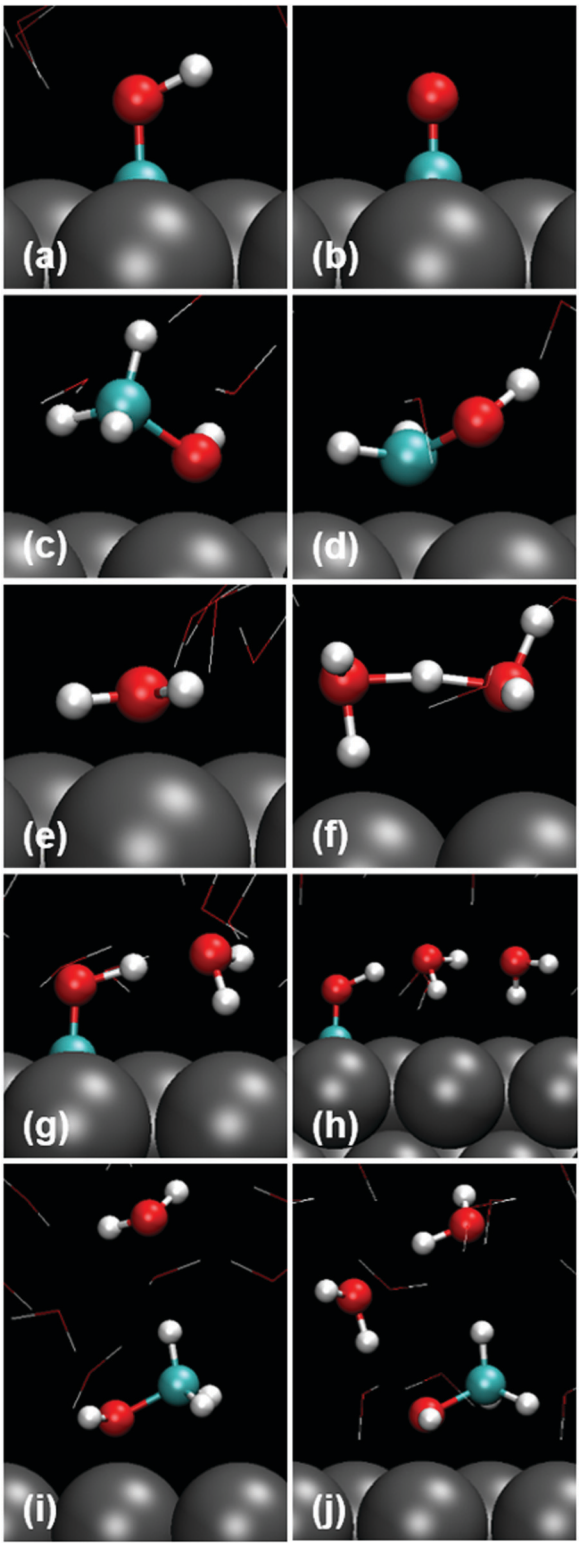

Fig. 1 Geometries of (a) COH*, (b) CO*, (c) CH_3OH*, (d) CH_2OH*, (e) H_2O, (f) H_5O_2, (g) COH–H_2O*, (h) COH–H_2O–H_2O*, (i) CH_3OH–H_2O*, and (j) CH_3OH–H_2O–H_2O* on Pt(111) under liquid H_2O. Liquid water molecules are drawn as lines for visual clarity. Gray = Pt, teal = C, red = O, and white = H.

(6) (*i.e.*, CH_3OH* + * → CH_2OH* + H*), (7) (*i.e.*, CH_3OH* + H_2O → CH_3OH–H_2O*), and (9) (*i.e.*, CH_3OH–H_2O–H_2O* → CH_2OH* + H_5O_2)

Table 1 Calculated interaction energies in units of eV

Reaction intermediate or TS	ΔE_{int} [eV]
COH*	−0.70 ± 0.07
CO*	−0.03 ± 0.03
COH–H_2O*	−0.55 ± 0.09
COH–H_2O–H_2O*	−1.07 ± 0.17
CH_3OH*	−0.48 ± 0.18
CH_2OH*	−0.64 ± 0.12
CH_3OH–H_2O*	−1.29 ± 0.20
CH_3OH–H_2O–H_2O*	−1.27 ± 0.29
H*	0.00 ± 0.00
* (vacant Pt site)	0[a]
H_2O	−0.28 ± 0.10
H_5O_2	−1.50 ± 0.31
TS, reaction 1	−0.01 ± 0.16
TS, reaction 3	−0.64 ± 0.10
TS, reaction 5	−1.12 ± 0.08
TS, reaction 6	−0.58 ± 0.15
TS, reaction 9	−0.89 ± 0.18
TS, reaction 10	−0.74 ± 0.21

[a] This value is 0 by definition.

fall into this category. The magnitudes of $\Delta\Delta E_{int}$ are significant at >0.25 eV for reactions (1), (2), (5) and (7)–(10), indicating significant influence of the liquid H_2O environment on the energies of these reactions. Further, ΔE_{rxn}^{vac} and $\Delta\Delta E_{int}$ directly counteract each other for reactions (1)–(3), (5) and (7)–(10). Of these, the sign on ΔE_{rxn}^{aq} is opposite of that on ΔE_{rxn}^{aq} for all but reaction (2), indicating the ability of the liquid H_2O environment to alter the energetic favorabilities of these reactions.

3.3 Transition states and activation energies

Calculated TS structures are shown in Fig. 4, and activation barriers are reported in Table 2 and plotted in Fig. 3. For reactions (1), (5), (6) and (10), the H_2O environment has a similar influence on ΔE_{act}^{aq} *via* $\Delta\Delta E_{int}$ as for ΔE_{rxn}^{aq}, whereas it has an opposite influence for reactions (2) and (9). $\Delta\Delta E_{int}$ for reactions (1), (9) and (10) are positive, meaning that $\Delta E_{act}^{aq} > \Delta E_{act}^{vac}$, while $\Delta\Delta E_{int}$ for reactions (3), (5), and (6) are negative, meaning that $\Delta E_{act}^{aq} < \Delta E_{act}^{vac}$. The magnitudes of $\Delta\Delta E_{int}$ are significant at >0.25 eV for reactions (1), (9) and (10), indicating that the liquid H_2O environment significantly influences the kinetics of these reactions.

Two of the activation barriers plotted in Fig. 3 are negative. ΔE_{act}^{aq} for reaction (3) is negative because ΔE_{act}^{vac} for this reaction

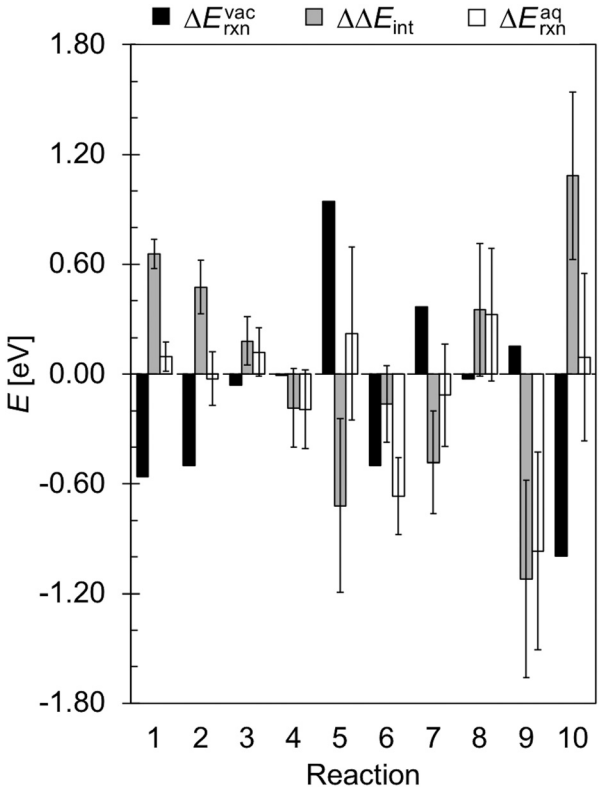

Fig. 2 Calculated ΔE_{rxn}^{vac} (black bars), $\Delta\Delta E_{int}$ (gray bars), and ΔE_{rxn}^{aq} (white bars) in units of eV.

is ∼0 and $\Delta\Delta E_{int}$ is ∼−0.10 eV; however, the average value of ΔE_{act}^{aq} is within the 95% confidence interval on $\Delta\Delta E_{int}$. For reaction (10), the TS complex was calculated to be lower in energy than the reactants in vacuum phase, suggesting that in vacuum phase, this reaction is not activated. In aqueous phase, ΔE_{act}^{aq} for reaction (10) is positive (albeit small).

3.4 Pre-exponential factors

Calculated pre-exponential factors, A, are reported in Table 2. For reactions where we assumed the pre-exponential factor is k_BT/h, $A = 10^{12}$ s^{-1} at the simulated temperature of 300 K. Reactions (2) and (7), *i.e.*, where a liquid H_2O molecule forms a

Table 2 Calculated reaction energies (ΔE_{rxn}^{aq}), activation energies (ΔE_{act}^{aq}), and pre-exponential factors (A_{for})

No.	Reaction[a]	ΔE_{rxn}^{aq} [eV]	ΔE_{act}^{aq} [eV]	A_{for} [s^{-1}]
1	COH* + * → CO* + H*	0.10 ± 0.08	1.68 ± 0.18	6.25×10^{12}
2a	COH* + H_2O → COH–H_2O*(d)	−0.02 ± 0.15	[b]	$(1.43 \pm 0.21) \times 10^{10}$
2b	COH* + H_2O → COH–H_2O*	,,	[b]	$(4.04 \pm 0.03) \times 10^{12}$
3	COH–H_2O*(d) + * → CO* + H* + H_2O	0.12 ± 0.13	−0.09 ± 0.13	6.25×10^{12}
4	COH–H_2O* + H_2O → COH–H_2O–H_2O*	−0.19 ± 0.22	[b]	6.25×10^{12}
5	COH–H_2O–H_2O* → CO* + H_5O_2	0.22 ± 0.47	0.07 ± 0.19	6.25×10^{12}
6	CH_3OH* + * → CH_2OH* + H*	−0.67 ± 0.21	0.34 ± 0.23	6.25×10^{12}
7a	CH_3OH* + H_2O → CH_3OH–H_2O*(d)	−0.11 ± 0.28	[b]	$(3.00 \pm 1.24) \times 10^{8}$
7b	CH_3OH* + H_2O → CH_3OH–H_2O*	,,	[b]	$(6.87 \pm 0.70) \times 10^{9}$
8	CH_3OH–H_2O* + H_2O → CH_3OH–H_2O–H_2O*	0.33 ± 0.36	[b]	6.25×10^{12}
9	CH_3OH–H_2O–H_2O* → CH_2OH* + H_5O_2	−0.97 ± 0.52	1.23 ± 0.34	6.25×10^{12}
10	H_5O_2 + * → 2H_2O + H*	0.09 ± 0.46	0.07 ± 0.49	6.25×10^{12}

[a] (d) denotes the complex has a dangling hydrogen atom. [b] Did not calculate.

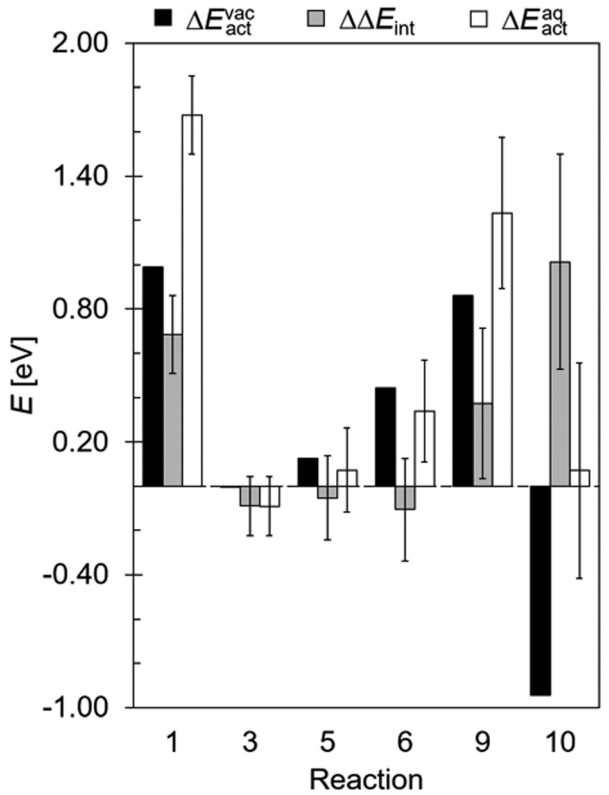

Fig. 3 Calculated ΔE_{act}^{vac} (black bars), $\Delta\Delta E_{int}$ (gray bars), and ΔE_{act}^{aq} (white bars) in units of eV.

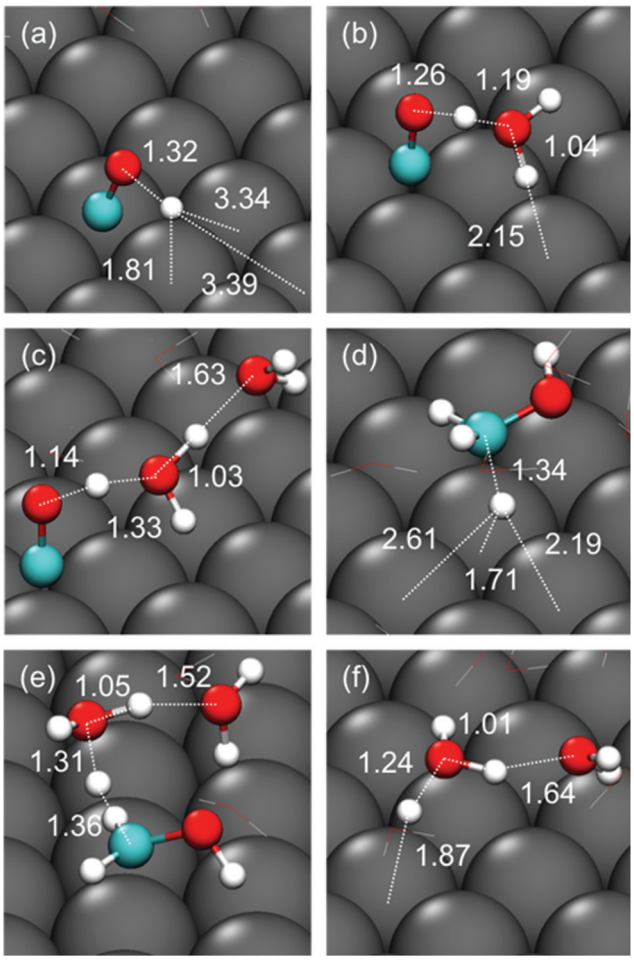

Fig. 4 Representative TS structures for (a) reaction (1), (b) reaction (3), (c) reaction (5), (d) reaction (6), (e) reaction (9), and (f) reaction (10). Water molecules not involved in the TS complex are displayed as lines for visual clarity. Gray = Pt, teal = C, red = O, and white = H.

complex with a COH* or CH_3OH* species, require the liquid H_2O structure to take on particular orientations. Since some orientations can promote co-catalyzed dehydrogenations, where the complexed H_2O molecule abstracts a hydrogen from COH* or CH_3OH* and simultaneously deposits a second hydrogen on the Pt(111) surface, we report two frequency factors for each of the complexation reactions in Table 2, one where the specific orientation could promote the co-catalyzed reaction (denoted "a" in Table 2) and one that generally describes the frequency of complexation and could promote co-catalyzed dehydrogenation or assisted dehyrogenation (denoted "b" in Table 2).

As the COH* species is highly hydrophilic (*i.e.*, having a ΔE_{int} of −0.70 eV), H_2O molecules frequently orient so as to complex with it; thus, the frequency of complexation between COH* and liquid H_2O is high, on the order of 10^{12} s^{-1}. The large pre-exponential factor for this reaction suggests that H_2O-mediated COH* dehydrogenation to CO* is feasible. As orientations that could promote the co-catalyzed pathway require that the complexed H_2O molecule have a dangling hydrogen atom, which is a specific case, the frequency of forming these complexes is smaller, on the order of 10^{10} s^{-1}. According to Table 2, ~0.4% of the COH–H_2O* complexes that form could promote H_2O-co-catalyzed dehydrogenation.

CH_3OH* also interacts strongly with H_2O, with $\Delta E_{int} = -0.48$ eV. However, this strong interaction energy is due to H_2O interactions with CH_3OH*'s –OH group, whereas in this manuscript, we are interested in the chemistry that occurs at the $-CH_3$ group. The $-CH_3$ group interacts significantly less favorably with H_2O, evidenced by the remarkably small pre-exponential factor for forming CH_3OH–H_2O* complexes at the $-CH_3$ group, which is on the order of 10^9 s^{-1}. The special case that could promote H_2O-co-catalyzed CH_3OH* dehydrogenation to CH_2OH* is even smaller, representing only ~4% of the total complexes that form at CH_3OH*'s $-CH_3$ group. Given that these pre-exponential factors are several orders of magnitude smaller than their non-H_2O-mediated analogs, CH_3OH* dehydrogenation to CH_2OH* likely occurs *via* the direct pathway.

4 Discussion

Taking the results from Sections 3.2, 3.3, and 3.4 together, the liquid H_2O environment inhibits the direct dehydrogenation of COH* (reaction (1), *i.e.*, COH* + * → CO* + H*). There are thermodynamic and kinetic penalties associated with breaking the O–H bond, since this results in a significantly weaker interaction with H_2O. In fact, ΔE_{act}^{aq} for this reaction is prohibitively high in liquid H_2O. In contrast, ΔE_{act}^{aq} for reactions involved in

H_2O-mediated COH* dehydrogenation are all <0.25 eV. Further, the pre-exponential factor for H_2O-mediated COH* dehydrogenation is competitive to that for the direct dehydrogenation reaction. Thus, COH* dehydrogenation to CO* in liquid H_2O likely occurs through a H_2O-mediated pathway. The liquid H_2O environment thus has a significant influence on the pathway for COH* dehydrogenation. In contrast, the liquid H_2O environment has a minor influence on the pathway for dehydrogenation of CH_3OH* to CH_2OH* (reaction (6) *i.e.*, $CH_3OH^* + * \rightarrow CH_2OH^* + H^*$). ΔE_{act}^{aq} for this reaction is significantly smaller at 0.34 eV than that for H_2O-mediated CH_3OH* dehydrogenation at 1.23 eV. Further, the frequencies of forming complexes that could lead to the H_2O-mediated CH_3OH* dehydrogenation to CH_2OH* are significantly smaller at 10^9 s^{-1} than those for the direct dehydrogenation reaction at 10^{12} s^{-1}. Hence, CH_3OH* dehydrogenation to CH_2OH* likely occurs through the direct pathway. These results are in agreement with isotopic labeling studies that have shown that water plays a role in catalytic O–H cleavage reactions but not C–H cleavage reactions.[53]

5 Conclusions

In this work, we used multiscale sampling to calculate reaction energies, activation energies, and pre-exponential factors for direct and H_2O-mediated dehydrogenation of COH* to CO* and CH_3OH* to CH_2OH*. We found that O–H cleavage is thermodynamically and kinetically inhibited in the aqueous phase compared to in vacuum. In fact, the direct dehydrogenation reaction becomes kinetically implausible, having an activation barrier of 1.7 eV. As the –OH group interacts favorably with H_2O, the O–H cleavage reaction can occur *via* a H_2O-mediated pathway. We find that the activation barrier for COH* dehydrogenation to CO* is <0.25 eV and that the pre-exponential term is high, on the order of 10^{12} s^{-1}. COH* dehydrogenation to CO* thus likely proceeds *via* a H_2O-mediated pathway. The liquid H_2O environment thus has a strong influence on COH* dehydrogenation to CO*, inhibiting the energetics of the direct pathway so significantly that the reaction proceeds *via* a H_2O-mediated route. In contrast, H_2O influences on C–H cleavage are much more minor. The H_2O-mediated pathway for this reaction is not competitive, having an activation barrier >1.0 eV and a pre-exponential factor that is three orders of magnitude smaller than the direct pathway. The H_2O environment thus does not directly participate in CH_3OH* dehydrogenation to CH_2OH* and instead only serves to provide energetic alterations. In this case, the H_2O environment improves both the reaction energy and the activation energy of the direct CH_3OH* to CH_2OH* reaction.

Conflicts of interest

There are no conflicts to declare.

Acknowledgements

This research was funding by the National Science Foundation through award number CBET-1438325. C. J. B. gratefully acknowledges fellowship support through NASA Training Grant NNX14AN43H. The authors also thank the Cyberinfrastructure Technology Integration (CITI) group at Clemson University for computational resources on the Palmetto Supercomputer Cluster.

References

1 L. C. Grabow, in *Computational Catalysis*, ed. A. Asthagiri and M. J. Janik, The Royal Society of Chemistry, 2014, pp. 1–57.
2 J. K. Nørskov, T. Bligaard, J. Rossmeisl and C. H. Christensen, *Nat. Chem.*, 2009, **1**, 37–46.
3 G. W. Huber, S. Iborra and A. Corma, *Chem. Rev.*, 2006, **106**, 4044–4098.
4 R. R. Davda, J. W. Shabaker, G. W. Huber, R. D. Cortright and J. A. Dumesic, *Appl. Catal., B*, 2005, **56**, 171–186.
5 G. W. Huber and J. A. Dumesic, *Catal. Today*, 2006, **111**, 119–132.
6 G. Pipitone, D. Tosches, S. Bensaid, A. Galia and R. Pirone, *Catal. Today*, 2018, **304**, 153–164.
7 A. Hamnett, *Catal. Today*, 2016, **38**, 445–457.
8 A. S. Arico, S. Srinivasan and V. Antonucci, *Fuel Cells*, 2001, **1**, 133–161.
9 H. Liu, C. Song, L. Zhang, J. Zhang, H. Wang and D. P. Wilkinson, *J. Power Sources*, 2006, **155**, 95–110.
10 J. Greeley and M. Mavrikakis, *Nat. Mater.*, 2004, **3**, 810–815.
11 X. Li and A. Faghri, *J. Power Sources*, 2013, **226**, 223–240.
12 J. Xuan, M. K. Leung, D. Y. Leung and M. Ni, *Renewable Sustainable Energy Rev.*, 2009, **13**, 1301–1313.
13 B. P. Chaplin, M. Reinhard, W. F. Schneider, C. Schüth, J. R. Shapley, T. J. Strathmann and C. J. Werth, *Environ. Sci. Technol.*, 2012, **46**, 3655–3670.
14 N. Barrabés and J. Sá, *Appl. Catal., B*, 2011, **104**, 1–5.
15 K. Kabra, R. Chaudhary and R. L. Sawhney, *Ind. Eng. Chem. Res.*, 2004, **43**, 7683–7696.
16 S. Ahmed, M. Rasul, W. N. Martens, R. Brown and M. Hashib, *Desalination*, 2010, **261**, 3–18.
17 M. Pelaez, N. T. Nolan, S. C. Pillai, M. K. Seery, P. Falaras, A. G. Kontos, P. S. Dunlop, J. W. Hamilton, J. Byrne, K. O'Shea, M. H. Entezari and D. D. Dionysiou, *Appl. Catal., B*, 2012, **125**, 331–349.
18 C. Li, X. Zhao, A. Wang, G. W. Huber and T. Zhang, *Chem. Rev.*, 2015, **115**, 11559–11624.
19 C.-R. Chang, Z.-Q. Huang and J. Li, *Wiley Interdiscip. Rev.: Comput. Mol. Sci.*, 2016, **6**, 679–693.
20 D. D. Hibbitts, B. T. Loveless, M. Neurock and E. Iglesia, *Angew. Chem., Int. Ed.*, 2013, **52**, 12273–12278.
21 V. Polshettiwar and R. S. Varma, *Green Chem.*, 2010, **12**, 743–754.
22 S. D. Ebbesen, B. L. Mojet and L. Lefferts, *J. Catal.*, 2007, **246**, 66–73.
23 C. J. Bodenschatz, S. Sarupria and R. B. Getman, *J. Phys. Chem. C*, 2015, **119**, 13642–13651.
24 Y. Okamoto, O. Sugino, Y. Mochizuki, T. Ikeshoji and Y. Morikawa, *Chem. Phys. Lett.*, 2003, **377**, 236–242.

25 D. Skachkov, C. Venkateswara Rao and Y. Ishikawa, *J. Phys. Chem. C*, 2013, **117**, 25451–25466.
26 S. Desai and M. Neurock, *Electrochim. Acta*, 2003, **48**, 3759–3773.
27 C. Hartnig and E. Spohr, *Chem. Phys.*, 2005, **319**, 185–191.
28 J. Liu, X.-M. Cao and P. Hu, *Phys. Chem. Chem. Phys.*, 2014, **16**, 4176–4185.
29 C. Michel, J. Zaffran, A. M. Ruppert, J. Matras-Michalska, M. Jedrzejczyk, J. Grams and P. Sautet, *Chem. Commun.*, 2014, **50**, 12450–12453.
30 C. Hartnig, J. Grimminger and E. Spohr, *J. Electroanal. Chem.*, 2007, **607**, 133–139.
31 Z.-Q. Huang, B. Long and C.-R. Chang, *Catal. Sci. Technol.*, 2015, **5**, 2935–2944.
32 C. Hartnig, J. Grimminger and E. Spohr, *Electrochim. Acta*, 2007, **52**, 2236–2243.
33 J. K. Nørskov, J. Rossmeisl, A. Logadottir, L. Lindqvist, J. R. Kitchin, T. Bligaard and H. Jonsson, *J. Phys. Chem. B*, 2004, **108**, 17886–17892.
34 R. Jinnouchi, K. Kodama and Y. Morimoto, *J. Electroanal. Chem.*, 2014, **716**, 31–44.
35 S. T. Dix, J. K. Scott, R. B. Getman and C. T. Campbell, *Faraday Discuss.*, 2016, **188**, 21–38.
36 M. Faheem, S. Suthirakun and A. Heyden, *J. Phys. Chem. C*, 2012, **116**, 22458–22462.
37 N. Artrith and A. M. Kolpak, *Nano Lett.*, 2014, **14**, 2670–2676.
38 M. Neurock, S. A. Wasileski and D. Mei, *Chem. Eng. Sci.*, 2004, **59**, 4703–4714.
39 J. A. Santana, C. R. Cabrera and Y. Ishikawa, *Phys. Chem. Chem. Phys.*, 2010, **12**, 9526–9534.
40 J. A. Herron, Y. M. Morikawa and M. Mavrikakis, *Proc. Natl. Acad. Sci. U. S. A.*, 2016, E4937–E4945.
41 H.-F. Wang and Z.-P. Liu, *J. Phys. Chem. C*, 2009, **113**, 17502–17508.
42 T. Xie, S. Sarupria and R. B. Getman, *Mol. Simul.*, 2017, **43**, 370–378.
43 T. Xie, C. J. Bodenschatz and R. B. Getman, *React. Chem. Eng.*, 2019, **4**, 383–392.
44 L. Bellarosa, R. García-Muelas, G. Revilla-López and N. López, *ACS Cent. Sci.*, 2016, **2**, 109–116.
45 X. Nie, W. Luo, M. Janik and A. Asthagiri, *J. Catal.*, 2014, **312**, 108–122.
46 M. J. Janik and M. Neurock, *Electrochim. Acta*, 2007, **52**, 5517–5528.
47 J. A. Santana, J. J. Mateo and Y. Ishikawa, *J. Phys. Chem. C*, 2010, **114**, 4995–5002.
48 J. A. Santana, J. J. Saavedra-Arias and Y. Ishikawa, *Electrocatalysis*, 2015, **6**, 534–543.
49 S. Behtash, J. Lu, M. Faheem and A. Heyden, *Green Chem.*, 2014, **16**, 605–616.
50 C. Michel and P. Gallezot, *ACS Catal.*, 2015, **5**, 4130–4132.
51 D. Cao, G.-Q. Lu, A. Wieckowski, S. A. Wasileski and M. Neurock, *J. Phys. Chem. B*, 2005, **109**, 11622–11633.
52 M. P. Hyman and J. W. Medlin, *J. Phys. Chem. B*, 2006, **110**, 15338–15344.
53 M. B. Boucher, M. D. Marcinkowski, M. L. Liriano, C. J. Murphy, E. A. Lewis, A. D. Jewell, M. F. G. Mattera, G. Kyriakou, M. Flytzani-Stephanopoulos and E. C. H. Sykes, *ACS Nano*, 2013, **7**, 6181–6187.
54 L. R. Merte, G. Peng, R. Bechstein, F. Rieboldt, C. A. Farberow, L. C. Grabow, W. Kudernatsch, S. Wendt, E. Lægsgaard, M. Mavrikakis and F. Besenbacher, *Science*, 2012, **336**, 889–893.
55 J. Saavedra, H. A. Doan, C. J. Pursell, L. C. Grabow and B. D. Chandler, *Science*, 2014, **345**, 1599–1602.
56 X. Zhang, T. E. Sewell, B. Glatz, S. Sarupria and R. B. Getman, *Catal. Today*, 2017, **285**, 57–64.
57 L. Árnadóttir, E. M. Stuve and H. Jónsson, *Chem. Phys. Lett.*, 2012, **541**, 32–38.
58 S. K. Desai, V. Pallassana and M. Neurock, *J. Phys. Chem. B*, 2001, **105**, 9171–9182.
59 A. J. R. Hensley, Y. Wang, D. Mei and J.-S. McEwen, *ACS Catal.*, 2018, **8**, 2200–2208.
60 C. J. Bodenschatz, X. Zhang, T. Xie, J. Arvay, S. Sarupria and R. B. Getman, *J. Visualized Exp.*, 2019, DOI: 10.3791/59284.
61 A. C. Van Duin, S. Dasgupta, F. Lorant and W. A. Goddard, *J. Phys. Chem. A*, 2001, **105**, 9396–9409.
62 Y. Wu, H. Chen, F. Wang, F. Paesani and G. A. Voth, *J. Phys. Chem. B*, 2008, **112**, 467–482.
63 Y. Han, D. Jiang, J. Zhang, W. Li, Z. Gan and J. Gu, *Front. Chem. Sci. Eng.*, 2016, **10**, 16–38.
64 A. Savara, I. Rossetti, C. E. Chan-Thaw, L. Prati and A. Villa, *ChemCatChem*, 2016, **8**, 2482–2491.
65 J. Greeley and M. Mavrikakis, *J. Am. Chem. Soc.*, 2004, **126**, 3910–3919.
66 H. Ogasawara, B. Brena, D. Nordlund, M. Nyberg, A. Pelmenschikov, L. Pettersson and A. Nilsson, *Phys. Rev. Lett.*, 2002, **89**, 276102.
67 G. Zimbitas, S. Haq and A. Hodgson, *J. Chem. Phys.*, 2005, **123**, 174701.
68 S. Haq, J. Harnett and A. Hodgson, *Surf. Sci.*, 2002, **505**, 171–182.
69 G. A. Kimmel, N. G. Petrik, Z. Dohnálek and B. D. Kay, *J. Chem. Phys.*, 2006, **125**, 044713.
70 M. J. Janik, C. D. Taylor and M. Neurock, *Top. Catal.*, 2007, **46**, 306–319.
71 Z. Cao, R. Kumar, Y. Peng and G. A. Voth, *J. Phys. Chem. C*, 2015, **119**, 14675–14682.
72 J.-S. Filhol and M.-L. Doublet, *Catal. Today*, 2013, **202**, 87–97.
73 E. S. Stoyanov, I. V. Stoyanova and C. A. Reed, *J. Am. Chem. Soc.*, 2010, **132**, 1484–1485.
74 A. Luzar and D. Chandler, *Nature*, 1996, **379**, 55–57.
75 J. Teixeira and M.-C. Bellissent-Funel, *J. Phys.: Condens. Matter*, 1990, **2**, SA105.
76 D. R. Lide, *CRC Handbook of Chemistry and Physics*, CRC Press, Boca Raton, FL, 1997, vol. 78.
77 S. Nosé, *Mol. Phys.*, 1984, **52**, 255–268.
78 W. G. Hoover, *Phys. Rev. A: At., Mol., Opt. Phys.*, 1985, **31**, 1695–1697.
79 S. Plimpton, *J. Comput. Phys.*, 1995, **117**, 1–19.
80 A. K. Rappé, C. J. Casewit, K. Colwell, W. Goddard III and W. Skiff, *J. Am. Chem. Soc.*, 1992, **114**, 10024–10035.

81 K. Kahn and T. C. Bruice, *J. Comput. Chem.*, 2002, **23**, 977–996.
82 A. D. MacKerell, D. Bashford, M. Bellott, R. Dunbrack, J. D. Evanseck, M. J. Field, S. Fischer, J. Gao, H. Guo and S. Ha, *et al.*, *J. Phys. Chem. B*, 1998, **102**, 3586–3616.
83 H. Lorentz, *Ann. Phys.*, 1881, **248**, 127–136.
84 D. Berthelot, *Comptes Rendus*, 1898, **126**, 1703–1706.
85 X. Zhang, R. S. DeFever, S. Sarupria and R. B. Getman, *J. Chem. Inf. Model.*, 2019, DOI: 10.1021/acs.jcim.9b00089.
86 G. Kresse and J. Hafner, *Phys. Rev. B: Condens. Matter Mater. Phys.*, 1993, **47**, 558.
87 G. Kresse and J. Hafner, *Phys. Rev. B: Condens. Matter Mater. Phys.*, 1994, **49**, 14251.
88 G. Kresse and J. Furthmüller, *Comput. Mater. Sci.*, 1996, **6**, 15–50.
89 G. Kresse and J. Furthmüller, *Phys. Rev. B: Condens. Matter Mater. Phys.*, 1996, **54**, 11169.
90 P. E. Blöchl, *Phys. Rev. B: Condens. Matter Mater. Phys.*, 1994, **50**, 17953.
91 G. Kresse and D. Joubert, *Phys. Rev. B: Condens. Matter Mater. Phys.*, 1999, **59**, 1758.
92 J. P. Perdew, K. Burke and M. Ernzerhof, *Phys. Rev. Lett.*, 1996, **77**, 3865.
93 J. P. Perdew, K. Burke and M. Ernzerhof, *Phys. Rev. Lett.*, 1997, **78**, 1396.
94 S. Grimme, *J. Comput. Chem.*, 2006, **27**, 1787–1799.
95 H. J. Monkhorst and J. D. Pack, *Phys. Rev. B: Condens. Matter Mater. Phys.*, 1976, **13**, 5188.
96 P. Pulay, *Chem. Phys. Lett.*, 1980, **73**, 393–398.
97 G. Henkelman and H. Jonsson, *J. Chem. Phys.*, 2000, **113**, 9901–9904.
98 G. Henkelman and H. Jonsson, *J. Chem. Phys.*, 2000, **113**, 9978–9985.
99 G. Henkelman and H. Jonsson, *J. Chem. Phys.*, 1999, **111**, 7010.
100 G. Henkelman, VASP TST Tools, http://theory.cm.utexas.edu/vtsttools/, accessed: 09-26-2017.

